


Cite this: *RSC Adv.*, 2018, 8, 35386

Antibacterial properties of electrospun $\text{Ti}_3\text{C}_2\text{T}_z$ (MXene)/chitosan nanofibers†

 Elisa A. Mayerberger,‡ Reva M. Street,‡ Riki M. McDaniel, Michel W. Barsoum
and Caroline L. Schauer *

Electrospun natural polymeric bandages are highly desirable due to their low-cost, biodegradability, non-toxicity and antimicrobial properties. Functionalization of these nanofibrous mats with two-dimensional nanomaterials is an attractive strategy to enhance the antibacterial effects. Herein, we demonstrate an electrospinning process to produce encapsulated delaminated $\text{Ti}_3\text{C}_2\text{T}_z$ (MXene) flakes within chitosan nanofibers for passive antibacterial wound dressing applications. *In vitro* antibacterial studies were performed on crosslinked $\text{Ti}_3\text{C}_2\text{T}_z$ /chitosan composite fibers against Gram-negative *Escherichia coli* (*E. coli*) and Gram-positive *Staphylococcus aureus* (*S. aureus*) – demonstrating a 95% and 62% reduction in colony forming units, respectively, following 4 h of treatment with the 0.75 wt% $\text{Ti}_3\text{C}_2\text{T}_z$ – loaded nanofibers. Cytotoxicity studies to determine biocompatibility of the nanofibers indicated the antibacterial MXene/chitosan nanofibers are non-toxic. The incorporation of $\text{Ti}_3\text{C}_2\text{T}_z$ single flakes on fiber morphology was analyzed by scanning electron microscopy (SEM) and transmission electron microscopy equipped with an energy-dispersive detector (TEM-EDS). Our results suggest that the electrospun $\text{Ti}_3\text{C}_2\text{T}_z$ /chitosan nanofibers are a promising candidate material in wound healing applications.

Received 24th July 2018
Accepted 1st October 2018

DOI: 10.1039/c8ra06274a

rsc.li/rsc-advances

1. Introduction

With the discovery of graphene, a two-dimensional (2D) material comprised of a single atomic layer of sp^2 bonded carbons, interest in 2D materials suitable for biomedical applications has grown due to their inherent antibacterial activity, impressive mechanical properties, and thermal stability.^{1–4} MXenes—a family of 2D transition metal layered hexagonal ternary carbides and/or nitrides—have attracted a great deal of attention for applications including supercapacitors,^{5,6} batteries,^{7–9} water purification,^{10–12} catalysis,^{13–15} and desalination.¹⁶ These materials have a $\text{M}_{n+1}\text{X}_n\text{T}_z$ composition, where M is an early transition metal, X is carbon or nitrogen, $n = 1, 2$, or 3, and T is a variable surface termination (*i.e.* OH, F, O, Cl).^{6,7,17} Currently there are only a few studies on the antibacterial behavior of MXene, predominantly for use as antibiofouling agents in wastewater treatment.^{18,19} However, the antibacterial properties of MXene for their potential use as medical bandaging materials have yet to be studied.

As MXenes are nanoscale materials, usually manufactured in colloidal suspension, a carrier polymer is required for accurate dosage and immobilization for use as a medical bandage.

Electrospun nanofibers are an ideal carrier medium, as they exhibit desirable characteristics such as high surface area and porosity, flexibility in chemical functionalization, excellent permeability and high absorption capabilities.²⁰ Chitosan (CS), a polysaccharide derivative of chitin, was chosen as a carrier polymer due to its biocompatibility, biodegradability, and low-cost. CS is a natural polymer that has been used in numerous studies for biomedical applications including drug-delivery systems, tissue engineering, wound healing, and antibacterial effects derived from its cationic nature.^{21–27} While electrospinning and crosslinking of chitosan is possible,^{28,29} most studies of electrospun chitosan for antibacterial applications use a copolymer to increase stability and electrospinnability.^{30–32} In this study, $\text{Ti}_3\text{C}_2\text{T}_z$ (MXene) delaminated single and few layer flakes was electrospun within chitosan nanofibers for the first time. Only recently has MXene been successfully incorporated within electrospun polymers such as poly(acrylic acid) (PAA), poly(ethylene oxide) (PEO), poly(vinyl alcohol) (PVA), and alginate/PEO.³³

Electrospun polymers functionalized with two-dimensional materials (*i.e.* graphene oxide (GO),^{34–37} exfoliated nanosheets of metal-organic frameworks (MOFs),³⁸ transition-metal dichalcogenides (TMDCs),³⁹ and layered zeolites⁴⁰) and their antibacterial activities have been extensively studied. Chitosan/poly(lactide-co-glycolide) (PLGA) functionalized with GO decorated with silver nanoparticles *via* a two-step process displayed excellent antibacterial activity to Gram-negative (*E. coli* and *P. aeruginosa*) (inactivation rate of 99%) and Gram-positive (*S.*

Department of Materials Science and Engineering, Drexel University, Philadelphia, PA 19104, USA. E-mail: cls52@drexel.edu

† Electronic supplementary information (ESI) available. See DOI: 10.1039/c8ra06274a

‡ Indicates equal contribution.



aureus) bacteria (inactivation rate of 76%).³⁴ Antibacterial properties of electrospun GO sheets that were blended directly with PVA/chitosan displayed clear zones of inhibition, whose mean diameter increased with increasing GO loading.³⁵ Previous studies attribute the antibacterial mechanism of GO to oxidative and physical stresses, including production of reactive oxygen species (ROS) and penetration of the bacterial membrane by the two-dimensional sharp edges.⁴¹ Similarly, the antibacterial effects of $\text{Ti}_3\text{C}_2\text{T}_z$ flakes and membranes have been suggested to be due to their sharp edges, high surface hydrophilicity and action as a reducing agent.^{18,19} The antibacterial activity of $\text{Ti}_3\text{C}_2\text{T}_z$ incorporated within electrospun nanofibers as a bandage medium; however, has never been studied.

In this study, we report on the fabrication of glutaraldehyde-crosslinked and basified $\text{Ti}_3\text{C}_2\text{T}_z/\text{CS}$ nanofibers produced by electrospinning a blend of the natural polymer CS and delaminated $\text{Ti}_3\text{C}_2\text{T}_z$ single and few-layer flakes colloidal suspensions. To realize the potential bandage applications of $\text{Ti}_3\text{C}_2\text{T}_z/\text{CS}$, the antibacterial effects of the nanofibers on the Gram-negative *Escherichia coli* (*E. coli*) and the Gram-positive *Staphylococcus aureus* (*S. aureus*) were studied. This work shows that even with a low $\text{Ti}_3\text{C}_2\text{T}_z$ concentration in the composite (less than 1.0 wt%), substantial antibacterial activity is achieved.

2. Results and discussion

2.1 Synthesis and characterization of $\text{Ti}_3\text{C}_2\text{T}_z$

$\text{Ti}_3\text{C}_2\text{T}_z$ is synthesized *via* the selective etching of Al layers from the starting material, Ti_3AlC_2 , using a LiF/HCl solution as an etchant as illustrated in (Fig. 1a). The resultant multilayered (ML) $\text{Ti}_3\text{C}_2\text{T}_z$ flakes are then washed with distilled water, centrifuged, and decanted to remove any remaining reaction by-products until a certain degree of spontaneous delamination occurs. A typical SEM image of the ML structure is shown in

(Fig. 1b). The ML $\text{Ti}_3\text{C}_2\text{T}_z$ is sonicated in water under a flow of a protective argon gas, to produce delaminated $\text{Ti}_3\text{C}_2\text{T}_z$, or a colloidal suspension of single and few-layer thick flakes as seen in (Fig. 1c and d), using SEM and TEM, respectively. The obtained $\text{Ti}_3\text{C}_2\text{T}_z$ flake sizes agreed with other studies following similar etching and delamination procedures.⁴²

A typical XRD pattern of a vacuum-assisted film of $\text{Ti}_3\text{C}_2\text{T}_z$ flakes displays a sharp, intense (002) peak at 6.9° . This peak corresponds to (00 l) basal-plane reflections with a c lattice parameter of 25 Å, indicative of the presence of water and Li cations between the negatively charged sheets.¹⁷ For this study, the antibacterial properties of delaminated $\text{Ti}_3\text{C}_2\text{T}_z$ composites were investigated due to the previously demonstrated antibacterial effects of the flakes.

2.2 Morphology and structure of $\text{Ti}_3\text{C}_2\text{T}_z/\text{CS}$ nanofiber mats

2.2.1. $\text{Ti}_3\text{C}_2\text{T}_z/\text{CS}$ fiber morphology. SEM micrographs (Fig. 2a) show the as-spun CS mats with uniform, cylindrical fibers with an average fiber diameter of 211 ± 40 nm. Fine-tuning of electrospinning parameters led to consistent formation of uniform CS nanofibers with $\text{Ti}_3\text{C}_2\text{T}_z$ loads of 0, 0.05, 0.10, 0.25, 0.50, and 0.75 wt%. These $\text{Ti}_3\text{C}_2\text{T}_z$ concentrations were chosen because they consistently formed uniform, bead-free nanofibers. SEM micrographs of the $\text{Ti}_3\text{C}_2\text{T}_z/\text{CS}$ nanofibers revealed the presence of dense networks of non-woven fibers of relatively uniform diameters (Fig. 2b–f). No branching of the fibers was observed, which suggests that the electrical forces and surface tension of the $\text{Ti}_3\text{C}_2\text{T}_z/\text{CS}$ solution during electrospinning were properly balanced. Morphology of the $\text{Ti}_3\text{C}_2\text{T}_z/\text{CS}$ nanofibers were visually comparable to those of the neat CS nanofibers. Average fiber diameters of the 0.05, 0.10, 0.25, 0.50, and 0.75 wt% $\text{Ti}_3\text{C}_2\text{T}_z/\text{CS}$ were 236 ± 59 , 170 ± 54 , 311 ± 144 , 279 ± 80 , and 298 ± 76 nm respectively (Fig. S1†). The data failed Levene's test for homogeneity at a significance level of

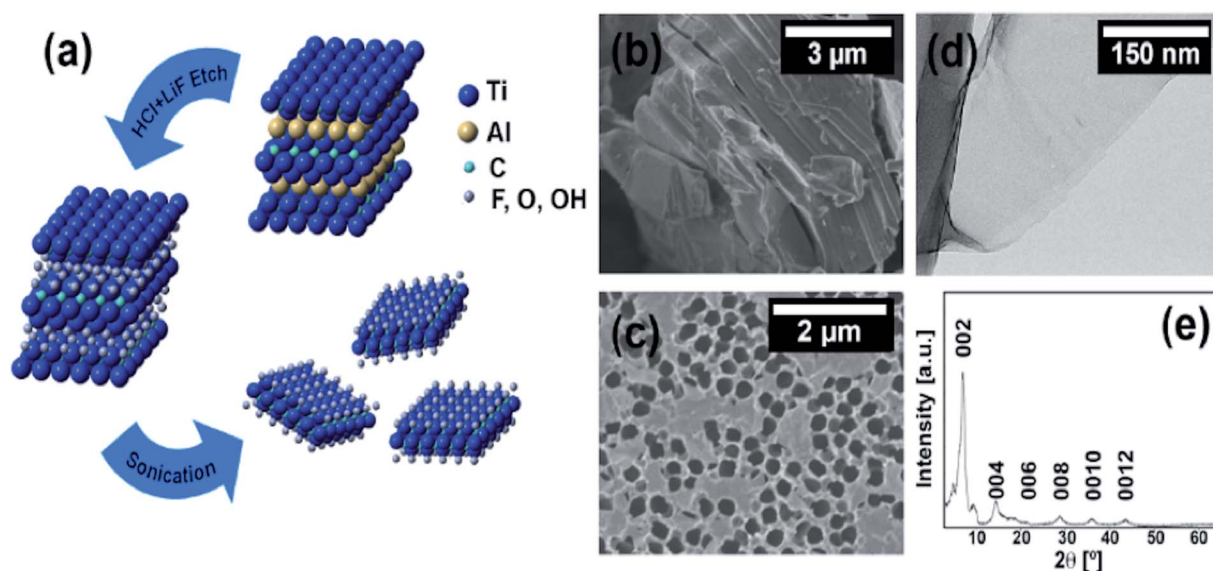


Fig. 1 (a) Schematic detailing the removal of the Al layers from the Ti_3AlC_2 to yield ML- $\text{Ti}_3\text{C}_2\text{T}_z$ that washing, and sonication then separate into individual $\text{Ti}_3\text{C}_2\text{T}_z$ flakes. (b) SEM micrographs of ML- $\text{Ti}_3\text{C}_2\text{T}_z$ powder and, (c) $\text{Ti}_3\text{C}_2\text{T}_z$ single and few-layer thick flakes on an anodized alumina membrane. (d) TEM micrograph of a $\text{Ti}_3\text{C}_2\text{T}_z$ flake. (e) XRD diffractogram of the vacuum assisted filtered $\text{Ti}_3\text{C}_2\text{T}_z$ film.



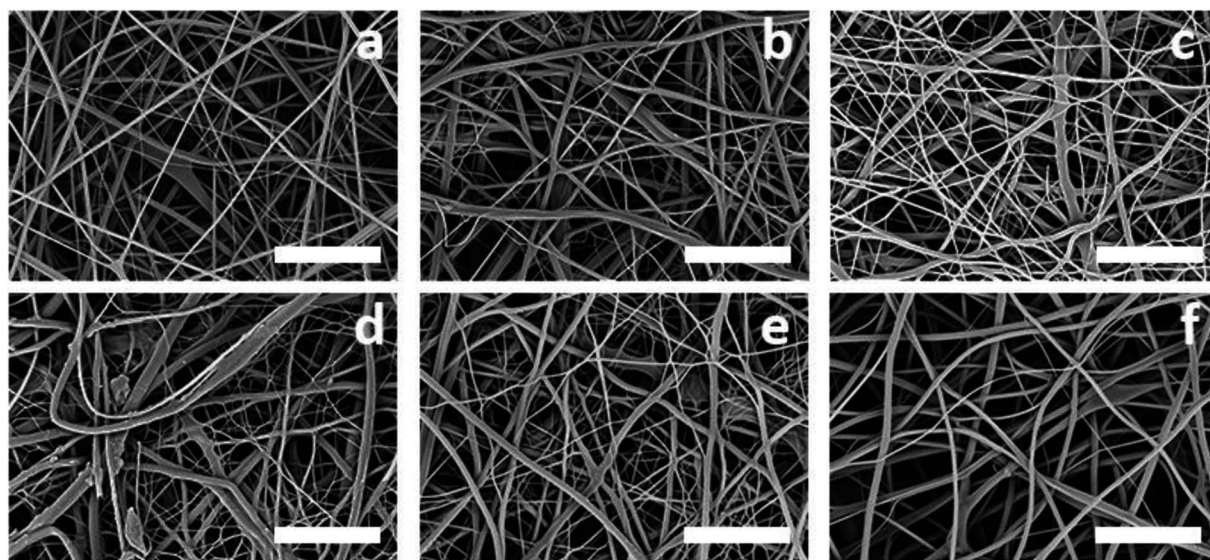


Fig. 2 SEM micrographs displaying the surface of the as-spun electrospun crosslinked $\text{Ti}_3\text{C}_2\text{T}_x/\text{CS}$ mats for the five different MXene loadings: (a) 0, (b) 0.05, (c) 0.10, (d) 0.25, (e) 0.50, and (f) 0.75 wt%. Scale bars represent 5 μm .

0.05, so a Kruskal–Wallis non-parametric analysis of variance (ANOVA) was performed, finding significant differences between fiber diameters at $p \leq 0.05$. Dunn's test was used for *post hoc* multiple comparison and indicated significant difference between the CS and the composite fibers containing 0.25, 0.50 and 0.75 wt% $\text{Ti}_3\text{C}_2\text{T}_x$. This difference in diameter may be due to the increasing water concentration in the electrospinning solutions from the increasing addition of $\text{Ti}_3\text{C}_2\text{T}_x$ aqueous suspensions.

2.2.2. $\text{Ti}_3\text{C}_2\text{T}_x/\text{CS}$ chemical functionalities. The chemical functionalities of as-spun CS and $\text{Ti}_3\text{C}_2\text{T}_x/\text{CS}$ fiber mats was investigated by FT-IR spectroscopy (Fig. 3a) to ensure that the addition of $\text{Ti}_3\text{C}_2\text{T}_x$ did not interfere in the crosslinking of the chitosan nanofibers. Typical CS bands at 3418 (hydroxyl group), 1203 (bridge ether oxygen), 1653 (amide I group), and 1532 cm^{-1} (amide II) appeared for all the nanofibrous mats (Table 1).⁴³ The amine deformation displayed in the FT-IR

spectra for both the neat and composite fibers indicates successful crosslinking, where glutaraldehyde undergoes a Schiff base reaction with the chitosan for the formation of an amine functionality and/or Michael-type adducts with terminal aldehydes to form carbonyl groups.⁴⁴ As shown by the negligible differences between the spectra of the neat and composite nanofibers, the crosslinking of the chitosan was unaffected by the addition of $\text{Ti}_3\text{C}_2\text{T}_x$.

2.2.3. $\text{Ti}_3\text{C}_2\text{T}_x/\text{CS}$ crystal structure. The effect of $\text{Ti}_3\text{C}_2\text{T}_x$ on the overall crystal structure of the CS nanofibers was investigated by X-ray diffraction (Fig. 3b). The neat CS and $\text{Ti}_3\text{C}_2\text{T}_x/\text{CS}$ nanofibers displayed similar XRD patterns with the typical amorphous broad reflection at 20.1° , signaling the retardation of the crystallization process of the chitosan blend.⁴⁵ However, the introduction of $\text{Ti}_3\text{C}_2\text{T}_x$ into chitosan nanofibers produced a somewhat broadened peak of decreased intensity, suggesting some form of interaction between the $\text{Ti}_3\text{C}_2\text{T}_x$ and CS. More specifically, $\text{Ti}_3\text{C}_2\text{T}_x$

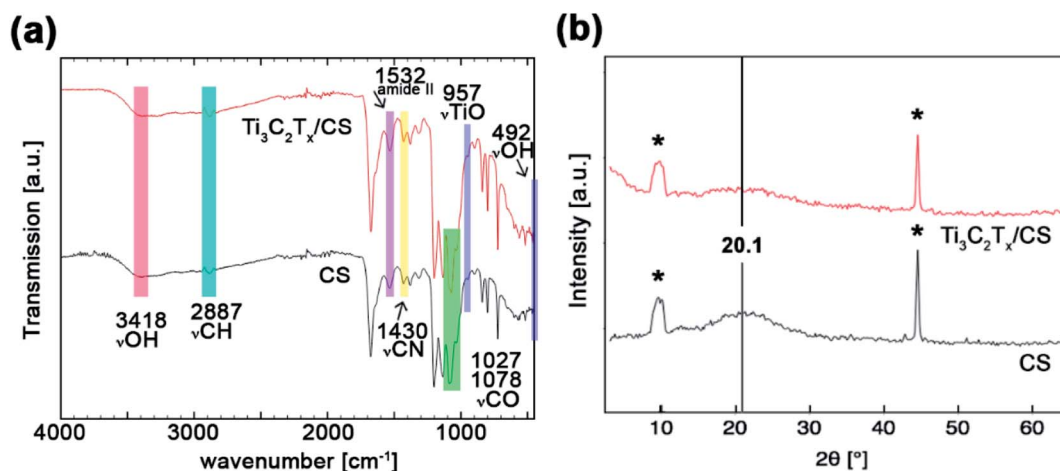


Fig. 3 (a) FTIR spectra and (b) XRD patterns of the neat chitosan nanofibers and the 0.75 wt% $\text{Ti}_3\text{C}_2\text{T}_x/\text{CS}$ nanofibers. Asterisks denote signal by the stage.



Table 1 FTIR peak annotations of the CS and $\text{Ti}_3\text{C}_2\text{T}_z/\text{CS}$ nanofibers

Peak frequency, cm^{-1}		Peak assignment	References
CS	$\text{Ti}_3\text{C}_2\text{T}_z/\text{CS}$		
3418	492, 3418	–OH stretching	28, 29, 46 and 62
—	957	Ti–O stretching	46 and 47
2887	2887	C–H stretching	28, 29, 46 and 62
1653	1653	Amide I	28, 29, 46 and 62
1532	1532	Amide II	28, 29, 46 and 62
1430	1430	C–N stretching	28, 29, 46 and 62
1203	1203	Bridge ether oxygen	28, 29, 46 and 62
1078, 1027	1078, 1027	C–O stretching	46 and 47

single flakes may physically interfere with the semi-crystalline behavior of CS *via* interfacial interactions and steric hindrance.⁴⁶

2.3 Characteristics of $\text{Ti}_3\text{C}_2\text{T}_z$ immobilized within CS nanofibers

Two different interactions are likely to occur at the organic-inorganic interface between the negatively charged surface terminations (O, F, OH, Cl) of the $\text{Ti}_3\text{C}_2\text{T}_z$ and the positively charged nitrogen-containing groups of chitosan. The first being electrostatic interactions and the second being the less dominant hydrogen bonding.^{47,48} Fig. 4a illustrates the orientations of $\text{Ti}_3\text{C}_2\text{T}_z$ to the CS nanofibers based on these interactions.

Due to the encapsulation of the $\text{Ti}_3\text{C}_2\text{T}_z$ flakes within the chitosan nanofibers, they could not be visualized from the SEM micrographs. To identify the presence of $\text{Ti}_3\text{C}_2\text{T}_z$ flakes, $\text{Ti}_3\text{C}_2\text{T}_z/\text{CS}$ fiber mats were analyzed by TEM (Fig. 4b). The TEM micrographs enabled the simultaneous visualization of the chitosan

nanofibers and the $\text{Ti}_3\text{C}_2\text{T}_z$ flakes. Two orientations were observed: full embodiment of the $\text{Ti}_3\text{C}_2\text{T}_z$ flake within the fiber and protrusion of the $\text{Ti}_3\text{C}_2\text{T}_z$ flake, as suggested in Fig. 4. The TEM-EDS micrograph and results on the composite fibers shows the presence of $\text{Ti}_3\text{C}_2\text{T}_z$ within the fiber (Fig. 4c). The chitosan was not doped and so the peaks for C and O are combined.

2.4 Antibacterial activity of electrospun $\text{Ti}_3\text{C}_2\text{T}_z/\text{CS}$ mats

2.4.1. GA crosslinked CS and $\text{Ti}_3\text{C}_2\text{T}_z/\text{CS}$. The antibacterial activity of the glutaraldehyde-crosslinked 0.75 wt% $\text{Ti}_3\text{C}_2\text{T}_z/\text{CS}$ composite nanofibers after 4 h of contact with *E. coli* and *S. aureus* is shown in (Fig. 5a and b). The glutaraldehyde-crosslinked $\text{Ti}_3\text{C}_2\text{T}_z/\text{CS}$ fibers exhibited a bacterial cell reduction of over 95% for *E. coli*, relative to the unmodified control CS fibers. A lower cell reduction of 62% was achieved against *S. aureus* due to the thicker peptidoglycan cell wall of Gram-positive bacteria which may provide protection against the antibacterial effects of the $\text{Ti}_3\text{C}_2\text{T}_z/\text{CS}$ composite nanofibers. Our results are in agreement with a previous study on PLGA/CS mats functionalized with silver nanoparticles, which reported higher cell reduction for *E. coli* than *S. aureus*.³⁴ The *E. coli* data passes Levene's test for homogeneity of variance (significance level of 0.05), so a one-way ANOVA with *post hoc* Tukey test was performed. The *S. aureus* data also does not pass Levene's test for homogeneity of variance (significance level of 0.05), so a Kruskal–Wallis one-way ANOVA with *post hoc* Dunn's test at significance level 0.05 was performed.

2.4.2. Basified CS and $\text{Ti}_3\text{C}_2\text{T}_z/\text{CS}$. Two methods of cross-linking, glutaraldehyde vapor deposition and basification, were used to compare the effect on the nanofiber antibacterial efficacy as a function of their crosslinking stability. Basification

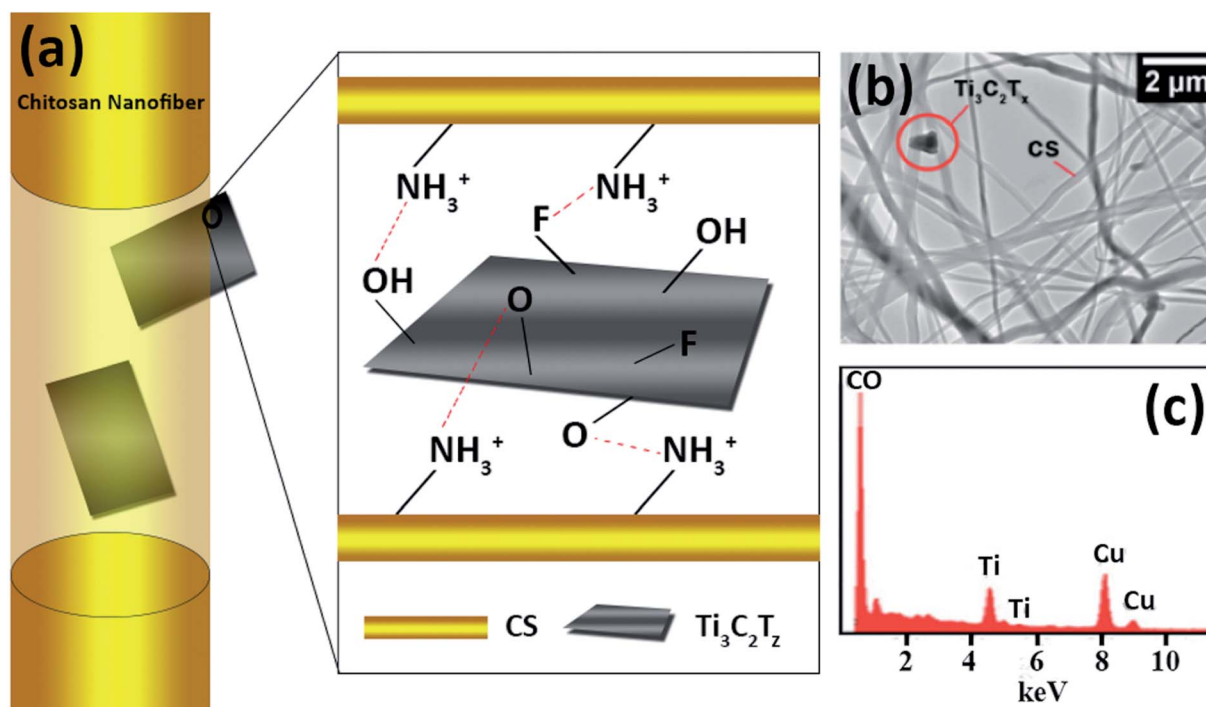


Fig. 4 (a) Schematic diagram illustrating the observed orientations of $\text{Ti}_3\text{C}_2\text{T}_z$ flakes within the chitosan nanofibers. (b) TEM micrograph of the $\text{Ti}_3\text{C}_2\text{T}_z/\text{CS}$ nanofibers and (c) elemental analysis (the presence of copper arises from the TEM grid).



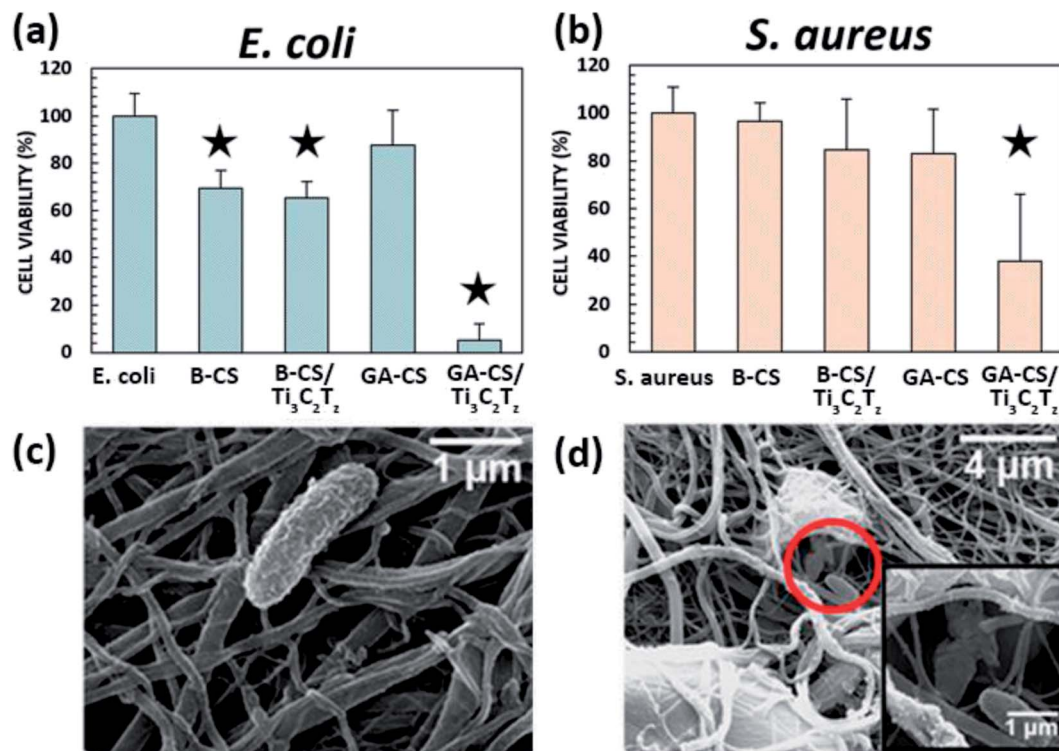


Fig. 5 Antibacterial activity of, (a) *E. coli* and (b) *S. aureus*. B-X and GA-X indicate mats treated with NaOH and glutaraldehyde, respectively. SEM micrographs shows an, (c) intact and, (d) destroyed *E. coli* bacteria on the 0.75 wt% $\text{Ti}_3\text{C}_2\text{T}_x/\text{CS}$ nanofiber mat. The star icon designates samples that are significantly different from the control, $p \leq 0.05$.

remains a common method for creating aqueous insoluble CS nanofiber mats *via* removal of the acetate salt. The application of NaOH neutralizes the amines on the chitosan, which prevents the mat from immediately dissolving into solution, but does not prevent the mat from beginning to degrade and smoothing into a film.⁴⁹

The basified composite proved to be effective against *E. coli* but showed less antibacterial activity against *S. aureus*, indicating that the charged NH_3 group may be required for *S. aureus* activity. While the mat did not disintegrate appreciably over the 4 h time period (measured *via* OD_{600} , data not shown), this smoothing effect may also have covered surface MXene flakes, reducing their efficacy against the *S. aureus* cell wall. Both basified CS and basified MXene composite nanofiber mats were effective against more susceptible *E. coli*, which may be due to the inherent antibacterial activity of CS. The mechanism is proposed to be direct adsorption of dissolved water-insoluble CS onto the surface of the bacterial cell, forming an impervious layer that blocks membrane transport channels and leads to cell death.⁵⁰ This is likely the same effect found in other studies of electrospun CS, as the combination of CS with a copolymer would not prevent bacteria from contacting regions of CS on the surface of the nanofibers.^{30–32}

2.4.3. Antibacterial mechanism. Following exposure to the $\text{Ti}_3\text{C}_2\text{T}_x/\text{CS}$ composite nanofibers, SEM micrographs of the attached cells were examined as shown in Fig. 5c and d. Morphological integrity was lost upon contact with the $\text{Ti}_3\text{C}_2\text{T}_x/\text{CS}$ mats as seen by the flattened and burst features of the

bacteria. These SEM micrographs are consistent with previous images obtained for *E. coli* following treatment with AgNPs.⁵¹

While there are many proposed mechanisms for the antibacterial nature of $\text{Ti}_3\text{C}_2\text{T}_x$ flakes,^{18,19} the most likely mechanisms involve direct contact of the bacteria with the MXene flakes. Direct mechanical destruction by MXene penetration through bacterial membranes has been observed by TEM,¹⁸ and is also considered to be the main cause of the antibacterial activity of two-dimensional GO.^{1–4,19} Additionally, the hydrophilic, negatively-charged flake surface (due to the reactive $-\text{OH}$, $-\text{F}$, and $-\text{O}$ surface terminations) may promote agglomeration of the bacteria, a significant indicator of antimicrobial activity in GO.⁵² Despite being incorporated into the nanofibers, the $\text{Ti}_3\text{C}_2\text{T}_x$ flakes retain a high degree of antibacterial effectiveness. Our findings compare well with other studies that tested $200 \mu\text{g mL}^{-1}$ $\text{Ti}_3\text{C}_2\text{T}_x$ colloidal suspensions against *E. coli* – resulting in a 99% bacterial inhibition.¹⁸

2.5 Biocompatibility of electrospun $\text{Ti}_3\text{C}_2\text{T}_x/\text{CS}$ mats

To determine the biocompatibility of $\text{Ti}_3\text{C}_2\text{T}_x/\text{CS}$ nanofibers, an *in vitro* cytotoxicity test was performed using HeLa cells, with results evaluated using an alamarBlue® assay. As shown in Fig. 6, the average cell viabilities relative to the control were over 85% at all test concentrations. The data passed Levene's test for homogeneity (at a significance level of 0.05), so a one-way analysis of variance (ANOVA) was performed, and no difference between samples was found ($p \leq 0.05$). This indicates that the mats are not cytotoxic to HeLa cells over 72 h of exposure.



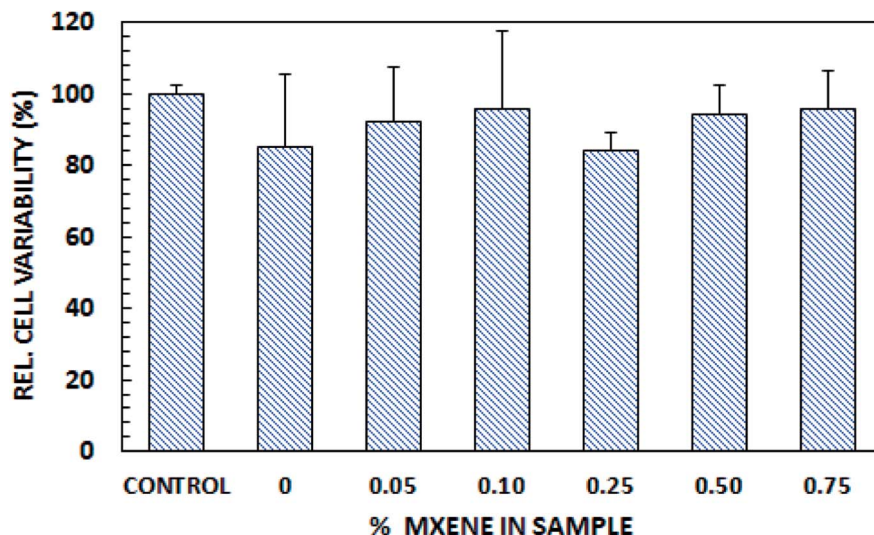


Fig. 6 Biocompatibility of $\text{Ti}_3\text{C}_2\text{T}_x/\text{CS}$ nanofibers.

2.6 Material comparison

A comprehensive literature review of electrospun materials with incorporated antibacterial two-dimensional and metal oxide nanoparticles (e.g. zinc oxide, titanium dioxide, and carbon nanotubes) clearly indicates that $\text{Ti}_3\text{C}_2\text{T}_x/\text{CS}$ nanofibers are the most effective in reducing *E. coli* and *S. aureus* at incredibly low doses (e.g. 0.75 wt% $\text{Ti}_3\text{C}_2\text{T}_x/\text{CS}$). Given that the most common application method for these nanoparticles is spraycoating or dipcoating onto the surface of electrospun fibers, their effectiveness may be lowered as the particles may be washed away in aqueous environments. Electrospinning a composite nanofiber, as detailed in this paper, allows the nanoparticles to be fully or partially encapsulated, limiting surface erosion.

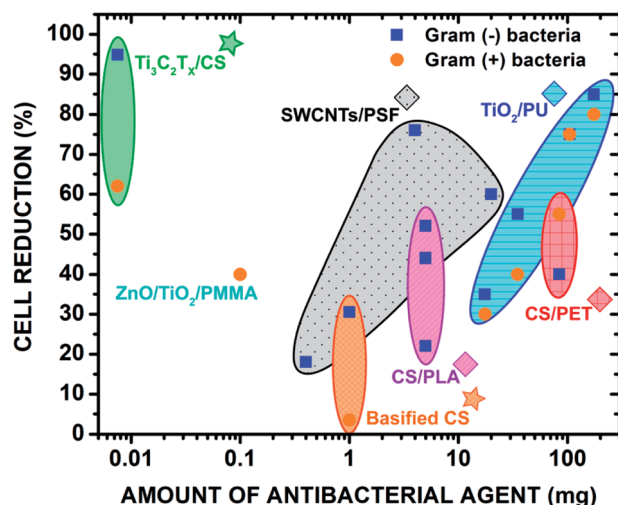


Fig. 7 Comparison of the antibacterial properties with the previous literature of select polymeric nanofibers with incorporated metal oxides and 2D materials. The antibacterial effects of electrospun polymer blends were also compared. The stars denote the materials from this study. Copyright WILEY-VCH Verlag GmbH & Co. KGaA, 69469 Weinheim, Germany, 2016.

Though 2D materials and metal oxides display excellent antibacterial properties, it is important to consider their biocompatibility for use in wound healing dressings. For example, GO at higher doses was shown to exhibit stark cytotoxicity reflected in the protrusion into mitochondrion and cell nuclei thus leading to apoptosis.⁵³ Carbon nanotubes have been found to promote inflammation and granuloma formation due to the formation of free radicals, release and accumulation of peroxidative products, depletion of antioxidant and oxidation of protein sulfhydryl groups.^{54,55} TiO_2 was revealed to be toxic to the cells of major organs such as the brain and liver, causing acute necrosis. It was also demonstrated that TiO_2 was capable of travelling through the placental barrier of pregnant mice and relaying neurotoxicity to their offspring.⁵⁶ Despite these properties displayed by commonly studied 2D materials and metal oxides, $\text{Ti}_3\text{C}_2\text{T}_x$ encapsulated by the chitosan nanofibers proved to be non-toxic. This is supported by previous studies demonstrating the high biocompatibilities of $\text{MnO}_x/\text{Ti}_3\text{C}_2$ composite materials and functionalized Ti_3C_2 nanosheets with GdW_{10} -based polyoxometalates (POMS) (Fig. 7).^{57,58}

3. Conclusions

We present the functionalization of electrospun CS nanofiber mats with $\text{Ti}_3\text{C}_2\text{T}_x$ flakes to develop flexible bandage materials with antimicrobial properties. $\text{Ti}_3\text{C}_2\text{T}_x$ flakes were successfully incorporated into chitosan nanofibers without alteration to the nanofiber integrity as confirmed by SEM and TEM. Contact with the $\text{Ti}_3\text{C}_2\text{T}_x/\text{CS}$ nanofiber surface imparted remarkable antibacterial activity, leading to a cell reduction rate of 95% against Gram-negative (*E. coli*) and 62% against Gram-positive (*S. aureus*) bacteria. Our findings strongly suggest the application of $\text{Ti}_3\text{C}_2\text{T}_x/\text{CS}$ nanofiber mats as excellent wound dressing materials.



4. Experimental

4.1 Materials

Medium molecular weight chitosan with 77% deacetylation ($M_w = 190\text{--}310$ kDa), glutaraldehyde solution (50%), ethanol (EtOH, 99.5%), sodium hydroxide (NaOH), phosphate buffered saline (PBS), glycine and hydrochloric acid (HCl, 37.0%) were obtained from Sigma Aldrich. Lithium fluoride (LiF, 99% trace metals basis) and trifluoroacetic acid (TFA, 99%) were obtained from Alfa Aesar. Sodium chloride (NaCl), BD Bacto™ Agar and yeast extract were purchased from Fisher Scientific and Tryptone from Oxoid. NEB® 5- α competent *Escherichia coli* was purchased from New England Biolabs and *Staphylococcus aureus* subsp. *aureus* Rosenbach was purchased from American Type Culture Collection (ATCC).

4.2 Synthesis and characterization of MXene ($\text{Ti}_3\text{C}_2\text{T}_z$)

A colloidal suspension of $\text{Ti}_3\text{C}_2\text{T}_z$ flakes was obtained *via* sonication of multilayer $\text{Ti}_3\text{C}_2\text{T}_z$, after etching the MAX phase Ti_3AlC_2 in a LiF/HCl solution as described previously.⁴² Briefly, Ti_3AlC_2 (1.0 g) was gradually added to 12 M HCl solution (10 mL) containing LiF (1.0 g) and left to stir for 24 h at 35 °C. The solution was then washed five to eight times with deionized (DI) water *via* a procedure of agitation, centrifugation (3500 rpm/ $2301 \times g$ for 2 min), and decantation, until the supernatant became dark in color. The solution was then sonicated in ice water for 1 h under flowing argon gas and centrifuged (5000 rpm/ $4696 \times g$ for 1 h). Information regarding the morphological properties of $\text{Ti}_3\text{C}_2\text{T}_z$ flakes was obtained through scanning electron microscopy (SEM) (Zeiss Supra 50VP SEM) and transmission electron microscopy (TEM) (JEOL JEM2100) operating at an accelerating voltage of 200 kV. Samples for the TEM, started as $\text{Ti}_3\text{C}_2\text{T}_z$ flakes in a colloidal suspension, were diluted 1 : 20 in DI water, sonicated for 10 min in a water bath, and drop-cast onto copper aperture grids. Samples were allowed to fully dry before imaging. X-ray diffraction (XRD) patterns of a free-standing membrane comprised of $\text{Ti}_3\text{C}_2\text{T}_z$ flakes were acquired with a Rigaku Smartlab with Cu K radiation with step size of 0.04 degrees and dwell time of 0.7 s per step.

4.3 Fabrication of $\text{Ti}_3\text{C}_2\text{T}_z$ /CS nanofibers

Chitosan solutions 2.7% (w/v) were prepared in trifluoroacetic acid (TFA), and then loaded with MXene at 0, 0.05, 0.10, 0.25, 0.50 or 0.75 wt% based on the solid CS.²⁸ The solution was rotated overnight or until uniform. The electrospinning setup was comprised of a high voltage power supply (20–25 kV), a syringe and metal needle (5 mL; 21 gauge), with a tip-to-copper collector distance of 10–14 cm. All solutions were pumped at 1 mL h^{−1} at room temperature (23.0 ± 0.5 °C) and under 9–15% relative humidity. The glutaraldehyde-crosslinked samples were prepared by exposing the electrospun fibers to glutaraldehyde vapor for 24 h in an airtight chamber.^{28,29,59} The basified samples were prepared by soaking in 1 M NaOH in EtOH for 0.5 h, then washed in changes of ethanol until the pH returned to neutral as measured *via* litmus paper.

4.4 Characterization of as-spun and crosslinked nanofibers

Fourier transform infrared spectroscopy (FTIR) spectra were recorded from 4000 to 400 cm^{−1} using a Perkin Elmer Spectrum Two FTIR spectrometer. X-ray diffraction (XRD) patterns of the fiber mats were acquired with a Rigaku Smartlab with Cu K radiation with step size of 0.04 degrees and dwell time of 0.7 s per step. Nanofiber morphology and size was examined in a SEM (Zeiss Supra 50VP) using an accelerating voltage of 3.50 kV. Average fiber diameters were calculated from fifty measurements per sample using ImageJ software.⁶⁰ A TEM (JEOL JEM2100) equipped with an ultrathin window energy-dispersive detector (TEM-EDS) was used to identify $\text{Ti}_3\text{C}_2\text{T}_z$ within the chitosan nanofibers using an accelerating voltage of 200 kV. Samples were prepared by placing them on a copper aperture grid. The hydrophilicity of the fiber surface was evaluated by measuring the water contact angle.

4.5 Antibacterial tests

To prepare for testing, the electrospun mats were weighed into 1.0 ± 0.1 mg samples and soaked in EtOH for 1 h to sterilize them ($n = 4$ per type). The EtOH was then removed, and the mats were allowed to dry completely under sterile conditions. The glutaraldehyde-crosslinked mats then had residual reactive aldehyde groups capped using a sterile saturated glycine solution. Finally, the mats were washed and conditioned in 3 changes of sterile $1 \times$ PBS. The bacterial strains were inoculated and cultured in sterilized lysogeny broth (LB) overnight in a shaking incubator at 37 °C. The cultures were then diluted to $\sim 3 \times 10^8$ CFU mL^{−1} in sterile PBS, corresponding to an OD₆₀₀ of 0.375 ± 0.02 for *E. coli* and OD₆₀₀ of 0.200 ± 0.02 for *S. aureus*. Both bacteria solutions were then diluted 1 : 1000 in sterile PBS to a concentration of $\sim 3 \times 10^5$ CFU mL^{−1}, and 1 mL of this bacteria solution was combined with each sterile electrospun mat. All samples were prepared using sterile techniques and cultured in a shaking incubator at 37 °C for 4 h. The same volume of bacteria, without electrospun mats, was also incubated as a control. The antibacterial activity of the electrospun samples was assessed using the spread plate method.⁶¹ At 4 h incubation time, a serial dilution of each sample was plated onto LB agar plates using sterile techniques and incubated in a still incubator at 37 °C overnight. Following incubation, the colonies were counted using a Bio-Rad ChemiDoc™ MP System and Quantity One® 1-D analysis software with manual verification of each colony count. The dilution used for the spread plate method was previously determined and found to be within the statistically relevant range.⁶¹ The antibacterial effect was calculated relative to the controls containing no electrospun mats. After contact with the electrospun mats, the morphology of the attached bacteria cells was observed using a SEM. The fibers were first rinsed with sterile PBS pH 6.8 and fixed using 2.5% paraformaldehyde/2.5% glutaraldehyde diluted in 0.2 M Sorenson's buffer pH 7.2 for several hours. A series of water-ethanol treatments (50 : 50, 30 : 70, 20 : 80, 10 : 90, and 100 ethanol) for 10 min each were used to dehydrate the attached cells. The fibers were then dried at room temperature.



4.6 Cytotoxicity studies using mammalian cells

Cytotoxicity of the glutaraldehyde-crosslinked bandages was measured using HeLa cells cultured in complete Dulbecco's Modified Eagle Medium (DMEM supplemented with 10% fetal bovine serum (FBS) and 1% penicillin/streptomycin). Samples (1.0 ± 0.1 mg, $n = 4$ per type) had reactive aldehydes capped using a saturated glycine solution as detailed previously, and then were sterilized using EtOH and dried under UV light. Samples were added to a 24-well plate well containing 5×10^4 HeLa cells in 1.5 mL complete DMEM. The cells were then cultured for 72 h at 37 °C and 5% CO₂. A negative control of the cells with no bandages present was also prepared. Cell viability was assessed using an alamarBlue® assay by first removing media and bandages from the well, adding 1.5 mL warmed complete media containing 10% alamarBlue® and incubating them for 4 h at 37 °C protected from light. The number of live cells was assessed by measuring absorbance at 570 nm, normalized to the 600 nm reading value. Cell viability was calculated relative to the control wells.

Conflicts of interest

There are no conflicts to declare.

Acknowledgements

The authors wish to acknowledge the entire Habas research lab at Temple University for assistance with bacterial studies. Furthermore, the authors would like to thank S. Kota and M. Ghidui for their extensive and useful discussions as well as the Drexel Centralized Research Facility, S. Huang, and A. Lang for assistance with TEM imaging. Funding for this work was provided by the Swedish Research Council (621-2014-4890).

References

- 1 D. Bitounis, H. Ali-Boucetta, B. H. Hong, D.-H. Min and K. Kostarelos, *Adv. Mater.*, 2013, **25**, 2258–2268.
- 2 C. Chung, Y.-K. Kim, D. Shin, S.-R. Ryoo, B. H. Hong and D.-H. Min, *Acc. Chem. Res.*, 2013, **46**, 2211–2224.
- 3 S. Gurunathan, J. W. Han, A. A. Dayem, V. Eppakayala and J.-H. Kim, *Int. J. Nanomed.*, 2012, **7**, 5901.
- 4 Y. Zhang, T. R. Nayak, H. Hong and W. Cai, *Nanoscale*, 2012, **4**, 3833–3842.
- 5 M. Naguib, O. Mashtalir, J. Carle, V. Presser, J. Lu, L. Hultman, Y. Gogotsi and M. W. Barsoum, *ACS Nano*, 2012, **6**, 1322–1331.
- 6 M. Naguib, M. Kurtoglu, V. Presser, J. Lu, J. Niu, M. Heon, L. Hultman, Y. Gogotsi and M. W. Barsoum, *Adv. Mater.*, 2011, **23**, 4248–4253.
- 7 M. Naguib, J. Come, B. Dyatkin, V. Presser, P.-L. Taberna, P. Simon, M. W. Barsoum and Y. Gogotsi, *Electrochem. Commun.*, 2012, **16**, 61–64.
- 8 M. Naguib, J. Halim, J. Lu, K. M. Cook, L. Hultman, Y. Gogotsi and M. W. Barsoum, *J. Am. Chem. Soc.*, 2013, **135**, 15966–15969.
- 9 D. Er, J. Li, M. Naguib, Y. Gogotsi and V. B. Shenoy, *ACS Appl. Mater. Interfaces*, 2014, **6**, 11173–11179.
- 10 Q. Peng, J. Guo, Q. Zhang, J. Xiang, B. Liu, A. Zhou, R. Liu and Y. Tian, *J. Am. Chem. Soc.*, 2014, **136**, 4113–4116.
- 11 Y. Ying, Y. Liu, X. Wang, Y. Mao, W. Cao, P. Hu and X. Peng, *ACS Appl. Mater. Interfaces*, 2015, **7**, 1795–1803.
- 12 O. Mashtalir, K. M. Cook, V. N. Mochalin, M. Crowe, M. W. Barsoum and Y. Gogotsi, *J. Mater. Chem. A*, 2014, **2**, 14334–14338.
- 13 Z. W. Seh, K. D. Fredrickson, B. Anasori, J. Kibsgaard, A. L. Strickler, M. R. Lukatskaya, Y. Gogotsi, T. F. Jaramillo and A. Vojvodic, *ACS Energy Lett.*, 2016, **1**, 589–594.
- 14 J. Ran, G. Gao, F.-T. Li, T.-Y. Ma, A. Du and S.-Z. Qiao, *Nat. Commun.*, 2017, **8**, 13907.
- 15 H. Pan, *Sci. Rep.*, 2016, **6**, 32531.
- 16 C. E. Ren, K. B. Hatzell, M. Alhabeab, Z. Ling, K. A. Mahmoud and Y. Gogotsi, *J. Phys. Chem. Lett.*, 2015, **6**, 4026–4031.
- 17 M. Ghidui, J. Halim, S. Kota, D. Bish, Y. Gogotsi and M. W. Barsoum, *Chem. Mater.*, 2016, **28**, 3507–3514.
- 18 K. Rasool, M. Helal, A. Ali, C. E. Ren, Y. Gogotsi and K. A. Mahmoud, *ACS Nano*, 2016, **10**, 3674–3684.
- 19 K. Rasool, K. A. Mahmoud, D. J. Johnson, M. Helal, G. R. Berdiyorov and Y. Gogotsi, *Sci. Rep.*, 2017, **7**, 1598.
- 20 S. Agarwal, J. H. Wendorff and A. Greiner, *Polymer*, 2008, **49**, 5603–5621.
- 21 R. Jayakumar, M. Prabakaran, S. V. Nair and H. Tamura, *Biotechnol. Adv.*, 2010, **28**, 142–150.
- 22 H. Ueno, T. Mori and T. Fujinaga, *Adv. Drug Delivery Rev.*, 2001, **52**, 105–115.
- 23 T. Dai, M. Tanaka, Y.-Y. Huang and M. R. Hamblin, *Expert Rev. Anti-Infect. Ther.*, 2011, **9**, 857–879.
- 24 J.-K. F. Suh and H. W. Matthew, *Biomaterials*, 2000, **21**, 2589–2598.
- 25 S. V. Madhally and H. W. Matthew, *Biomaterials*, 1999, **20**, 1133–1142.
- 26 J. D. Schiffman and C. L. Schauer, *Polym. Rev.*, 2008, **48**, 317–352.
- 27 E. I. Rabea, M. E.-T. Badawy, C. V. Stevens, G. Smagghe and W. Steurbaut, *Biomacromolecules*, 2003, **4**, 1457–1465.
- 28 J. D. Schiffman and C. L. Schauer, *Biomacromolecules*, 2007, **8**, 2665–2667.
- 29 J. D. Schiffman and C. L. Schauer, *Biomacromolecules*, 2007, **8**, 594–601.
- 30 A. Cooper, R. Oldinski, H. Ma, J. D. Bryers and M. Zhang, *Carbohydr. Polym.*, 2013, **92**, 254–259.
- 31 K.-H. Jung, M.-W. Huh, W. Meng, J. Yuan, S. H. Hyun, J.-S. Bae, S. M. Hudson and I.-K. Kang, *J. Appl. Polym. Sci.*, 2007, **105**, 2816–2823.
- 32 B. Son, B.-Y. Yeom, S. H. Song, C.-S. Lee and T. S. Hwang, *J. Appl. Polym. Sci.*, 2009, **111**, 2892–2899.
- 33 E. A. Mayerberger, O. Urbanek, R. M. McDaniel, R. M. Street, M. W. Barsoum and C. L. Schauer, *J. Appl. Polym. Sci.*, 2017, **134**(37), 45295.
- 34 A. F. De Faria, F. Perreault, E. Shaulsky, L. H. Arias Chavez and M. Elimelech, *ACS Appl. Mater. Interfaces*, 2015, **7**, 12751–12759.



- 35 Y. Liu, M. Park, H. K. Shin, B. Pant, J. Choi, Y. W. Park, J. Y. Lee, S.-J. Park and H.-Y. Kim, *J. Ind. Eng. Chem.*, 2014, **20**, 4415–4420.
- 36 H. R. Pant, C. H. Park, L. D. Tijing, A. Amarjargal, D.-H. Lee and C. S. Kim, *Colloids Surf., A*, 2012, **407**, 121–125.
- 37 Y. Y. Qi, Z. X. Tai, D. F. Sun, J. T. Chen, H. B. Ma, X. B. Yan, B. Liu and Q. J. Xue, *J. Appl. Polym. Sci.*, 2013, **127**, 1885–1894.
- 38 J. Quirós, K. Boltes, S. Aguado, R. G. de Villoria, J. J. Vilatela and R. Rosal, *Chem. Eng. J.*, 2015, **262**, 189–197.
- 39 S. Wu, J. Wang, L. Jin, Y. Li and Z. Wang, *ACS Appl. Nano Mater.*, 2018, **1**, 337–343.
- 40 K. A. Rieger, H. J. Cho, H. F. Yeung, W. Fan and J. D. Schiffman, *ACS Appl. Mater. Interfaces*, 2016, **8**, 3032–3040.
- 41 O. Akhavan and E. Ghaderi, *ACS Nano*, 2010, **4**, 5731–5736.
- 42 M. Ghidui, M. R. Lukatskaya, M.-Q. Zhao, Y. Gogotsi and M. W. Barsoum, *Nature*, 2014, **516**, 78.
- 43 A. Pawlak and M. Mucha, *Thermochim. Acta*, 2003, **396**, 153–166.
- 44 J. D. Schiffman and C. L. Schauer, *Biomacromolecules*, 2007, **8**, 2665–2667.
- 45 Y.-T. Jia, J. Gong, X.-H. Gu, H.-Y. Kim, J. Dong and X.-Y. Shen, *Carbohydr. Polym.*, 2007, **67**, 403–409.
- 46 Y. Liu, J. Zhang, X. Zhang, Y. Li and J. Wang, *ACS Appl. Mater. Interfaces*, 2016, **8**, 20352–20363.
- 47 M. Boota, M. Pasini, F. Galeotti, W. Porzio, M.-Q. Zhao, J. Halim and Y. Gogotsi, *Chem. Mater.*, 2017, **29**, 2731–2738.
- 48 O. Mashtalir, M. R. Lukatskaya, M.-Q. Zhao, M. W. Barsoum and Y. Gogotsi, *Adv. Mater.*, 2015, **27**, 3501–3506.
- 49 M. A. Kiechel and C. L. Schauer, *Carbohydr. Polym.*, 2013, **95**, 123–133.
- 50 C. Qin, H. Li, Q. Xiao, Y. Liu, J. Zhu and Y. Du, *Carbohydr. Polym.*, 2006, **63**, 367–374.
- 51 I. Sondi and B. Salopek-Sondi, *J. Colloid Interface Sci.*, 2004, **275**, 177–182.
- 52 S. Liu, T. H. Zeng, M. Hofmann, E. Burcombe, J. Wei, R. Jiang, J. Kong and Y. Chen, *ACS Nano*, 2011, **5**, 6971–6980.
- 53 K. Wang, J. Ruan, H. Song, J. Zhang, Y. Wo, S. Guo and D. Cui, *Nanoscale Res. Lett.*, 2011, **6**, 8.
- 54 A. Shvedova, V. Castranova, E. Kisin, D. Schwegler-Berry, A. Murray, V. Gandelsman, A. Maynard and P. Baron, *J. Toxicol. Environ. Health, Part A*, 2003, **66**, 1909–1926.
- 55 C. Salvador-Morales, E. Flahaut, E. Sim, J. Sloan, M. L. Green and R. B. Sim, *Mol. Immunol.*, 2006, **43**, 193–201.
- 56 P. Naserzadeh, F. Ghanbary, P. Ashtari, E. Seydi, K. Ashtari and M. Akbari, *J. Biomed. Mater. Res., Part A*, 2018, **106**, 580–589.
- 57 C. Dai, H. Lin, G. Xu, Z. Liu, R. Wu and Y. Chen, *Chem. Mater.*, 2017, **29**, 8637–8652.
- 58 L. Zong, H. Wu, H. Lin and Y. Chen, *Nano Res.*, 2018, 1–20.
- 59 A. E. Donius, M. A. Kiechel, C. L. Schauer and U. G. Wegst, *J. R. Soc., Interface*, 2013, **10**, 20120946.
- 60 W. S. Rasband, <http://imagej.nih.gov/ij>.
- 61 S. Sutton, *Journal of Validation Technology*, 2011, **17**, 42.
- 62 J. Brugnerotto, J. Lizardi, F. M. Goycoolea, W. Argüelles-Monal, J. Desbrieres and M. Rinaudo, *Polymer*, 2001, **42**, 3569–3580.

